crystals

MDPI

Article

Experimental and Computational Study of Microhardness Evolution in the HAZ for Al–Cu–Li Alloys

Stavroula Maritsa [1], Stavros Deligiannis [2], Petros E. Tsakiridis [2] and Anna D. Zervaki [1,*]

[1] Shipbuilding Technology Laboratory, School of Naval Architecture and Marine Engineering, National Technical University of Athens, Zografou, 157 80 Athens, Greece; maritsastavroula@mail.ntua.gr
[2] Laboratory of Physical Metallurgy, School of Mining and Metallurgical Engineering, National Technical University of Athens, Zografou, 157 80 Athens, Greece; stavrosdel@metal.ntua.gr (S.D.); ptsakiri@central.ntua.gr (P.E.T.)
* Correspondence: annazervaki@mail.ntua.gr; Tel.: +30-210-772-3691

Abstract: The Laser Beam Welding (LBW) of aluminum alloys has attracted significant interest from industrial sectors, including the shipbuilding, automotive and aeronautics industries, as it expects to contribute to significant cost reduction associated with the production of high-quality welds. To comprehend the behavior of welded structures in regard to their damage tolerance, the application of fracture mechanics serves as the instrumental tool. However, the methods employed overlook the changes in the microstructure within the Heat-Affected Zone (HAZ), which leads to the degradation of the mechanical properties of the material. The purpose of this study is to simulate microhardness evolution in the HAZ of AA2198-T351 LBW. The material represents the latest generation of Al-Cu-Li alloys, which exhibit improved mechanical properties, enhanced damage tolerance behavior, lower density and better corrosion and fatigue crack growth resistance than conventional Al-Cu alloys. In this work, the microhardness profile of LBW AA2198 was measured, and subsequently, through isothermal heat treatments on samples, the microhardness values of the HAZ were replicated. The conditions of the heat treatments (T, t) were selected in line with the thermal cycles that each area of the HAZ experienced during welding. ThermoCalc and DICTRA were employed in order to identify the strengthening precipitates and their evolution (dissolution and coarsening) during the weld thermal cycle. The microstructure of the heat-treated samples was studied employing LOM and TEM, and the strengthening precipitates and their characteristics (volume fraction and size) were defined and correlated to the calculations and the experimental conditions employed during welding. The main conclusion of this study is that it is feasible to imitate the microstructure evolution within the HAZ through the implementation of isothermal heat treatments. This implies that it is possible to fabricate samples for fatigue crack growth tests, enabling the experimental examination of the damage tolerance behavior in welded structures.

Keywords: laser beam welding; Al–Cu–Li alloys; heat affected zone; microstructure; microhardness

check for updates

Citation: Maritsa, S.; Deligiannis, S.; Tsakiridis, P.E.; Zervaki, A.D. Experimental and Computational Study of Microhardness Evolution in the HAZ for Al–Cu–Li Alloys. *Crystals* **2024**, *14*, 246. https://doi.org/10.3390/cryst14030246

Academic Editors: Reza Beygi, Mahmoud Moradi and Ali Khalfallah

Received: 21 February 2024
Revised: 26 February 2024
Accepted: 27 February 2024
Published: 1 March 2024

Copyright: © 2024 by the authors. Licensee MDPI, Basel, Switzerland. This article is an open access article distributed under the terms and conditions of the Creative Commons Attribution (CC BY) license (https://creativecommons.org/licenses/by/4.0/).

1. Introduction

Al–Cu–Li alloys have attracted strong interest from the industry due to their increased tensile strength, elastic modulus, fatigue resistance, ductility and lower density. [1–3]. Each 1 wt.% Li added to aluminum leads to a 3% decrease in density and a 6% increase in the elastic modulus. By adding 2 wt.% Li, the density of the alloy decreases by 10%, and the elastic modulus increases by 25–35% [2,4]. By replacing conventional high-strength Al alloys with Al–Li alloys, the structure's weight is reduced by 10–20%, and the elastic behavior is increased by 25–35% [4]. Therefore, these alloys are ideal materials for the aerospace and aeronautical industry, since the economic benefits are significant, such as increased payload and better fuel efficiency [5]. Furthermore, the potential Al–Li alloys exhibit in marine industry is significant [6,7].

In the third generation of Al–Li alloys, copper (Cu) content is increased (2–4 wt.%), while the amount of Li is reduced (0.75–1.8 wt.%). These alloys exhibit higher hardness, corrosion resistance, good crack propagation resistance and improved weldability [4,5,8–10]. Other micro-alloying elements, such as Mg, Mn, Zn, Ag, Zr and Fe, are added to improve mechanical strength. For example, Mg and Ag additions favor the formation of the T_1 phase, and the addition of Mg can stimulate the nucleation of GP zones [11]. The third generation of Al–Cu–Li alloys has been widely used as structural materials in the aerospace industry and has attracted significant research interest. These alloys are amenable to artificial aging heat treatment, leading to final products with increased strength and hardness. In addition, natural aging can be applied, during which the precipitates that are formed lead to improved ductility compared to artificial aging [4,12].

AA2198 is a popular widely used Al–Cu–Li alloy of this generation, exhibiting a good combination of hardness, corrosion resistance and ductility [2]. In the United States, alloy 2198-T8 (3.6–6.1 mm thick plate) has been successfully utilized for the construction of the Falcon 9 rocket to manufacture the primary and secondary fuel tanks and fairing components [4]. Furthermore, AA2198 belongs to the typical Al–Cu–Li grades that are widely used for the construction of aircrafts, such as A330/340/350/380 in Europe, Boeing 747/777/787 in America and Comac's C919 in China [13].

The hardness of AA2198 can be increased by natural or artificial aging due to the formation of strengthening precipitates, as overviewed in the Al-rich corner of the ternary Al–Cu–Li phase diagram given in Figure 1 [14]. A complex precipitation sequence has been observed during the aging process of Al–Cu–Li alloy systems. The precipitation sequence impacts the interaction mechanism between dislocations and precipitates during plastic deformation, consequently influencing the mechanical properties of the aged alloys [7,15]. Several precipitates have been observed through aging, including GP zones, θ′(Al_2Cu), β′(Al_3Zr), T_1(Al_2CuLi), δ′(Al_3Li) and S′(Al_2CuMg) [2,4,15,16]. The Li content has been found to be crucial in the precipitation of these alloys. High Li content (>2%) leads to a primary strengthening role attributed to δ′precipitates, with some contribution from S′, while lower Li content (<2%) results in T_1 being the primary strengthening precipitates, alongside minor θ′ [15,16]. Regarding the precipitation sequence of AA2198, where the Li content is low, a study [16] has shown that after natural aging, the microstructure is primarily composed of Cu-rich clusters, although they do not fit the description of single-layer Cu-rich GPI zones. When the temperature increases, these clusters become unstable and appear to dissolve entirely. The further increase of the temperature results in the artificial aging of AA2198 (155 °C/16 h in [16]) where the formation of T_1 initiates and becomes dominant, contributing to the alloy's strength. Additionally, other less prevalent precipitates are present, based on the Al–Cu sequence (GPI, GPII and θ′) [16]. The alloy's composition, especially the Cu/Li ratio is a dominant factor affecting the sequence. Furthermore, a higher Cu/Li ratio seems to produce a more rapid nucleation of T_1 in low-Li Al–Cu–Li alloys [16].

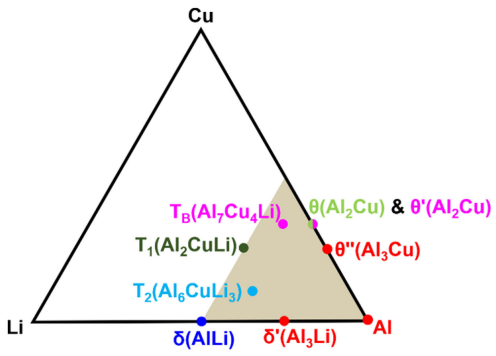

Figure 1. Al–Cu–Li ternary phase diagram near the Al-rich region. The different colors of the phases indicate their lattice (red: FCC, pink: cubic CaF_2, navy blue: BCC, green: BCT, olive green: hexagonal and sky blue: icosahedral). Reprinted/adapted with permission from Ref. [14]. 2024, Elsevier.

The introduction of welding in Al–Cu–Li alloy structures offers significant positive effects, such as lower weight and improved performance, while replacing conventional joining techniques [17,18]. Regarding the AA2198 alloy, two welding methods are usually utilized: Friction Stir Welding (FSW) [17,19–27] and laser welding methods [18,28–31]. Studies have confirmed the positive effect of micro-jet cooling for the welding of Al alloys [32,33]. Laser Beam Welding (LBW) is a popular method in the aerospace industry, as it offers high productivity, manufacturing flexibility and efficiency compared to other welding methods. Using the LBW method has proven that the total construction cost can be reduced by up to 40%, and a weight reduction of up to 28% can be achieved compared to conventional joining techniques [28]. In addition, LBW results in a narrower Heat-Affected Zone (HAZ) and a faster welding speed compared to FSW [29].

During the LBW of AA2198, a significant decrease in mechanical properties is observed near the Weld Zone (WZ) [17,34]. This is attributed to the fact that AA2198 is a heat-treatable alloy, and the mechanical properties depend mainly on the size and distribution of strengthening precipitates. The microstructural changes due to the welding thermal cycles, such as the coarsening or dissolution and re-precipitation of certain phases or precipitates, significantly affect the mechanical properties of an AA2198 weld [18]. Even after optimizing welding parameters, strength loss in alloy welds is considered inevitable [17]. During the welding of AA2198, the phases T1, δ′, S′ and θ′ are completely dissolved in the Al matrix, and after cooling, they re-precipitate [17,24]. The heterogeneous distributions of these phases in the HAZ depend on the local thermal cycles that the HAZ is subjected to [18].

The study of Fatigue Crack Growth (FCG) behavior in welds is of great importance, as it changes along the length of the weld seam due to the different thermal cycles to which the material is subjected. Studies have shown that the FCG rate is higher in the HAZ [35,36]. Investigating the mechanical and fatigue properties of the HAZ of a laser weld is a demanding task, due to the narrowness and heterogeneity of the region [37]. The main aim of this study is to simulate the reduction of the microhardness in the HAZ of an Al–Cu–Li 2198–T351 alloy by implementing several isothermal heat treatment schemes. This implies that it could be possible to fabricate samples that possess similar mechanical properties with different regions of the HAZ [38]. This, in turn, leads to the conclusion that these specimens could be subjected to FCG tests instead of the welds themselves [35,37,39].

2. Materials and Methods

2.1. Material and Experimental Procedure

The material to be studied is the AA2198–T351 Al–Cu–Li alloy in the form of a 3.8 mm thick sheet. The chemical composition of the alloy is shown in Table 1.

Table 1. Composition of AA2198 alloy (wt. %) in this study.

Si	Fe	Cu	Mn	Mg	Cr	Zn	Zr	Li	Ag	Al
0.08	0.10	3.50	0.5	0.80	0.05	0.35	0.18	1.10	0.50	Rem.

In this study, the Laser Beam Welding (LBW) method was utilized for the bead-on-plate welding of the alloy, with shielding gas 50% Ar (17.5 L/mm) and 50% He (17.5 L/mm) [40]. The welding conditions are shown in Table 2.

Table 2. AA2198 laser beam welding conditions.

Power (W)	Speed (m/min)	Heat Input Rate (J/mm)	Arc Efficiency
3441	2	103	0.47

During welding of the AA2198 alloy, various metallurgical phenomena occur in the HAZ, leading to its division into two sub-zones. The first will be referred to as HAZ_1, where

the maximum temperature exceeds the dissolution temperature of the main strengthening precipitates, causing them to dissolve completely and then re-precipitate. This phenomenon is equivalent to aging. The second one is HAZ_2, where the temperature is lower, and therefore, coarsening of the strengthening precipitates occurs, which is equivalent to over-aging. In fact, there is no exact boundary between these two regions; between them, a third sub-zone exists where both dissolution and coarsening occur simultaneously [41]. To simplify the problem in the present work, it will be assumed that the distinct boundary of the two sub-zones lies at the dissolution temperature of the main strengthening precipitate. To simulate the microhardness profile in the HAZ through isothermal heat treatments, appropriate aging and over-aging heat treatment schemes must be selected, which will be performed on samples sectioned from the parent material. Therefore, the microhardness values of HAZ_1 are replicated through solution heat treatments followed by natural aging, and those of HAZ_2 are replicated through over-aging heat treatments. This procedure is illustrated schematically in Figure 2. The conditions of the heat treatments, shown in Table 3, were selected in line with the Rosenthal solution model and DICTRA results, which are described in the next paragraph. Different temperatures were chosen for the solution heat treatment (450, 500 and 550 °C) to study whether the temperature affects the precipitation trend.

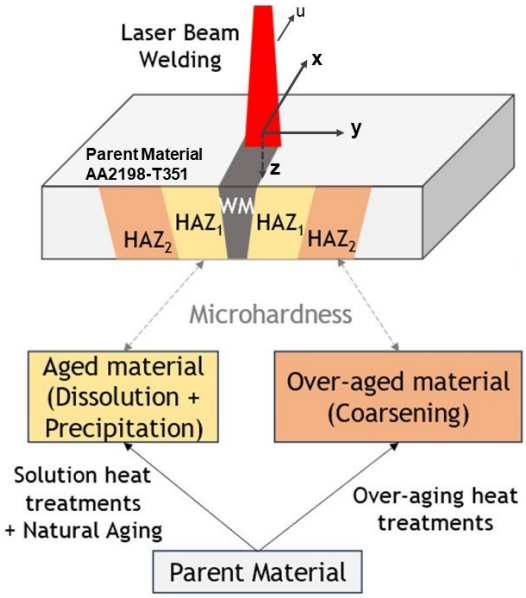

Figure 2. Schematic illustration of the experimental procedure in this study.

Table 3. Conditions (*T*,*t*) of the heat treatments carried out, followed by water quenching.

Solution Heat Treatment + Natural Aging	Over-Aging
450 °C/5, 10, 20, 40, 60 min	200 °C/8, 16, 24, 32, 48, 80, 153 h
500 °C/10, 20, 40, 60 min	250 °C/2, 4, 8, 16, 24, 32 h
550 °C/5, 10, 20, 40, 60 min	300 °C/8, 16 h

The heat-treated samples were metallographically prepared by embedding, grinding and polishing using 3 and 1 μm alumina paste. Keller's reagent was employed for etching the material. The microhardness measurements on the weld seam and the heat-treated samples were performed using the 402MVD Wolpert Wilson microhardness tester (Wilson Instruments, Norwood, MA, USA), with a load set at 0.2 kgf ($HV_{0.2}$) applied for 10 s. The macrostructure of the weld-seam was studied by utilizing a Leica Wilz M3Z stereoscope. The investigation of the precipitates formed during natural aging and over-aging was performed with a JEOL JEM-2100 LaB6 (JEOL Ltd., Tokyo, Japan) Transmission Electron

Microscope (TEM), operating at 200 kV. TEM specimens, with a 3 mm diameter, were prepared in the form of 30 μm-thick disk-type plates via mechanical polishing, followed by ion-polishing with a precision Ar-ion polishing system (PIPS) (Gatan model 691). Elemental analyses were carried out using an Oxford X-Max 100 Silicon Drift Energy Dispersive X-ray spectrometer (EDS) (Oxford Instruments, Abingdon, Oxfordshire, UK), connected to the TEM. Data were acquired in areas ranging from 2 to 5 nm in STEM mode.

2.2. Computational Procedure

A computational part preceded the experimental process in order to select the conditions of the heat treatments and predict the evolution of the main strengthening precipitates.

Thermocalc software (version 2022a, TCAL7 database) and Diffusion Module (DICTRA) (version 2022a, TCAL7/MOBAL5 databases) [42] were employed for the selection of the appropriate heat treatment time and the determination of the behavior of the main strengthening precipitates during the isothermal heat treatments.

Furthermore, the conditions of the heat treatments were chosen according to the thermal cycles the material was subjected to during welding. For this purpose, the Rosenthal solution (Equations (1)–(5)) [43] was implemented using suitable computing software. A coordinate (w, y, z) system is used (Figure 2), which moves at the same speed as the welding arc (u):

$$w = x - ut \tag{1}$$

$$T - T_o = \frac{Q}{2\pi k} e^{-\frac{u}{2\alpha}w} \left[\frac{e^{-\frac{u}{2\alpha}R}}{R} + \sum_{n=1}^{\infty} \left(\frac{e^{-\frac{u}{2\alpha}R_n}}{R_n} + \frac{e^{-\frac{u}{2\alpha}R'_n}}{R'_n} \right) \right] \tag{2}$$

$$R = \sqrt{w^2 + y^2 + z^2} \tag{3}$$

$$R_n = \sqrt{w^2 + y^2 + (2nH - z)^2} \tag{4}$$

$$R'_n = \sqrt{w^2 + y^2 + (2nH + z)^2} \tag{5}$$

The symbols used for the parameters are explained in Table 4.

Table 4. Model parameters and their numerical values.

Model Parameter (Unit)	Symbol	Numerical Value
Temperature (°C)	T	Calculated
Initial temperature (°C)	T_o	25
Arc thermal power (arc efficiency × power) (W)	Q	1617
Thermal conductivity (W/mm°C)	k	0.125
Arc speed (mm/s)	u	33.3
Thermal diffusivity (mm^2/s)	α	51.63
Thickness of Al sheet (mm)	H	3.8

Temperature field developed during LBW was calculated using Equation (2), entering the values depicted in Table 4. The results were validated via experimental observations regarding the boundary between the WM and the HAZ and are discussed in Section 3.2.

3. Results

3.1. Strengthening Precipitates and Their Evolution during the Welding Thermal Cycle

The boundary between HAZ_1 and HAZ_2 is set at the temperature at which the main strengthening precipitate(s) dissolve completely. For the AA2198, these are the T1, θ′ and δ′ precipitates. According to ThermoCalc calculations, the T1 and θ′ precipitates dissolve at 493 °C, so this temperature is chosen (Figure 3). Therefore, in Figure 3 the temperature boundaries of the two sub-zones are shown on the calculated phase diagram. The upper boundary of HAZ1 is set to the Liquidus Temperature (651 °C), whereas the lower boundary of HAZ_2 corresponds to the artificial aging temperature (175 °C).

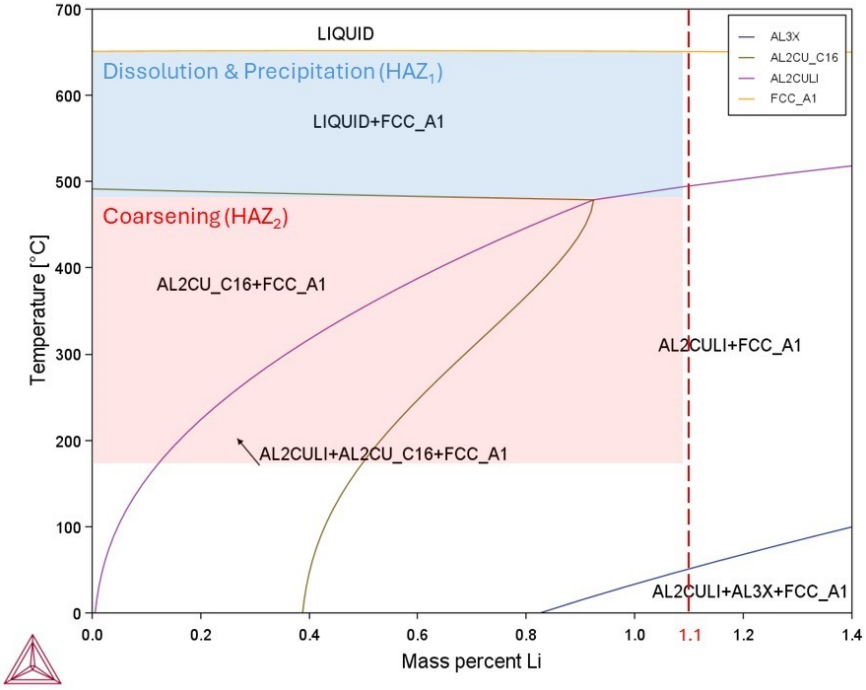

Figure 3. Calculated phase diagram for AA2198 alloy, along with the temperature boundaries of the two subzones HAZ_1 and HAZ_2.

The conditions of the isothermal heat treatments to replicate the microhardness reduction of these two zones were selected according to the Diffusion Module calculations. In HAZ_2 where coarsening takes place, temperatures ranging from 180 °C to 300 °C were tested with a step of 25 °C. As shown in Figure 4, as the temperature increases, the maximum diameter of θ′ increases. According to the calculations, the maximum diameter increases up to 63% at 300 °C in comparison with the initial mean diameter of θ′.

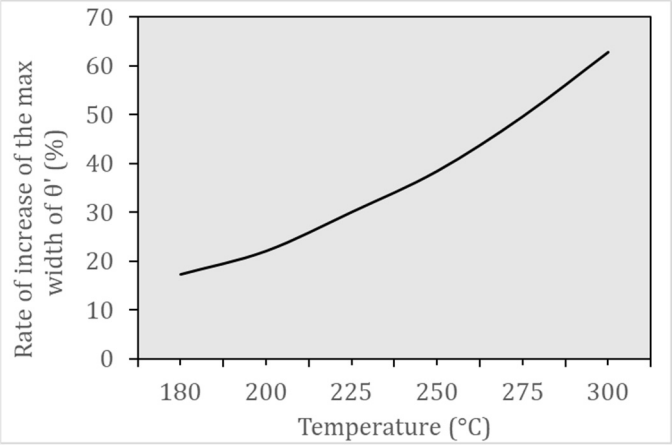

Figure 4. Rate of increase of the maximum width (nm) of the precipitate θ′ in relation to the initial width for various temperatures.

3.2. Temperature Field Developed during Welding

The calculated temperature field that develops in the sheet during LBW is shown in Figure 5a.

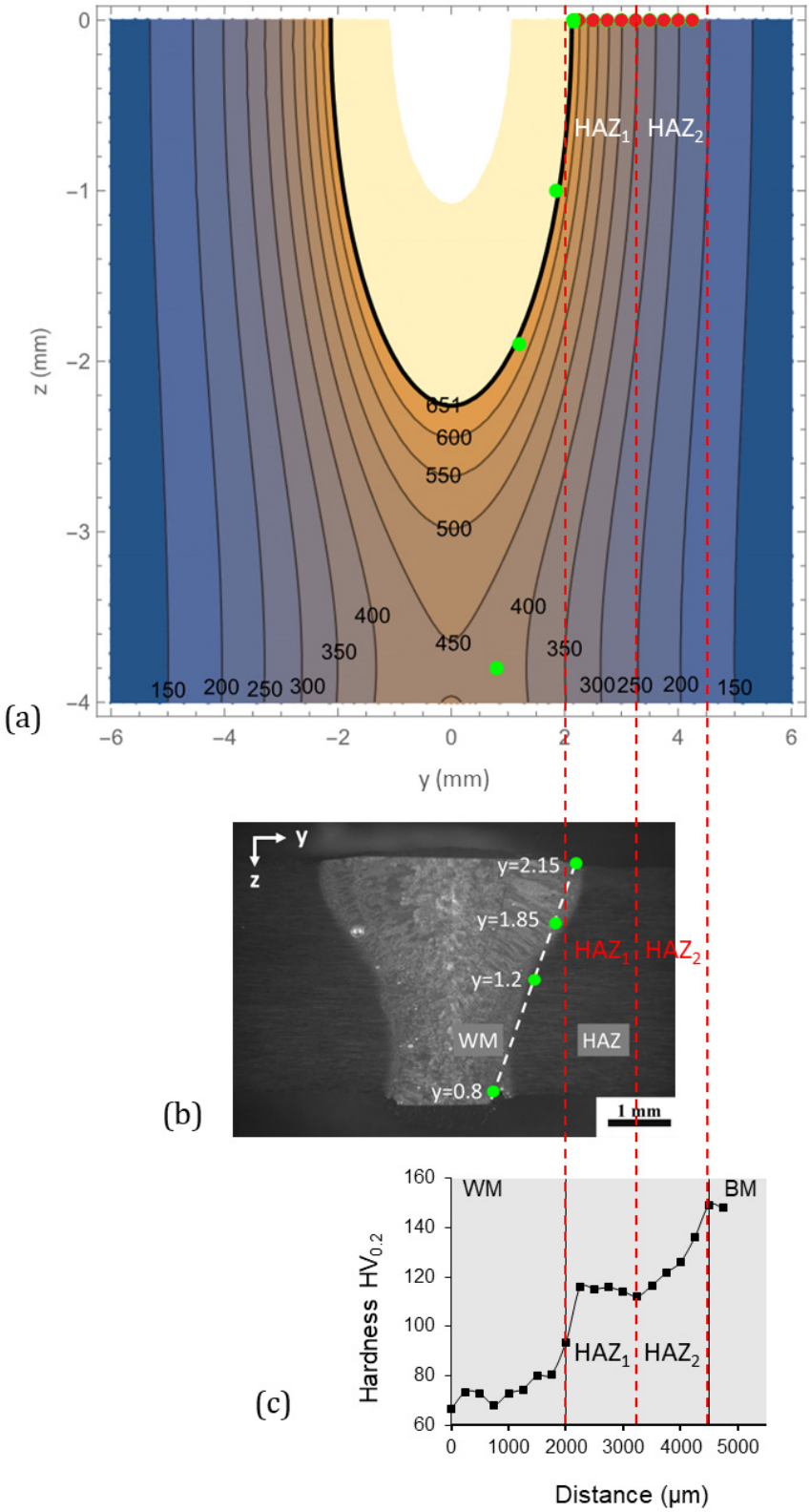

Figure 5. (**a**) Calculated temperature field in relation to the depth (z) and width (y) of the sheet, at x = 0. The green marks depict the experimental boundary between the WM and HAZ on the micrograph of the weld seam, while the red marks show the locations of the microhardness tests; (**b**) OM micrograph of the weld seam. Dashed line represents the WM/HAZ boundary where the max temperature during welding is equal to the liquidus, while the green marks on the boundary are the ones plotted in (**a**); (**c**) microhardness profile of the weld seam. The red dashed lines represent the comparison between the theoretical and experimental boundaries of HAZ_1 and HAZ_2.

In Figure 5a, the green dots depict the experimental points that lie on the actual boundary between the WM and the HAZ (Figure 5b), where the maximum temperature of the material during welding is equal to the liquidus (T_{liq} = 651 °C). The microhardness test results of the weld seam are presented in Figure 5c. The initial hardness of the material is 150 $HV_{0.2}$, while the microhardness decreases while moving from the center of the weld. Two sub-zones seem to be formed in the HAZ: the first at 2250–3250 μm where the microhardness value remains constant at approximately 115 $HV_{0.2}$ and the second at 3500–4250 μm, where the microhardness ranges between 116–136 $HV_{0.2}$.

As shown in Figure 6, the points on the experimental T_{liq} are very close to the points of the calculated T_{liq}, except for the last point (y = 0.8, z = 3.8). This is attributed to the fact that the Rosenthal solution does not take into account parameters such as the keyhole method that has been used. With this method, the arc reaches a greater depth in the material, which, however, cannot be predicted through the computational model. However, this does not negate the fact that the calculations correspond to the experimental data. The percentages in Figure 6 indicate the error divergence of the theoretical model in relation to the experimental data.

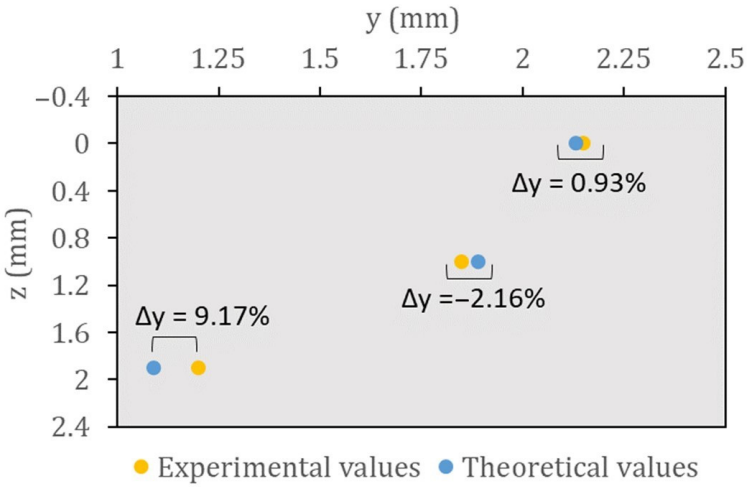

Figure 6. Comparison of the points on the experimental and theoretical WM/HAZ where the maximum temperature reached is equal to the T_{liq} = 651 °C. This indicates that the theoretical model is close to the real values, as the Δy% is relatively low.

Time is another parameter to consider in the calculations. Therefore, the thermal cycles to which different points of the HAZ are subjected are shown in Figure 7. These points are depicted in red in Figure 5a and are located at the surface of the sheet (z = 0 mm). At points from 2.25 to 3 mm, the temperature exceeds 493 °C during welding, causing the strengthening phases to dissolve completely and re-precipitate. At 3.25 mm, the temperature reaches up to 460 °C, resulting in a significant dissolution of the strengthening precipitates. Therefore, points 2.25 to 3.25 mm belong to HAZ_1 sub-zone. At points 3.5–4.25 mm, the temperature does not exceed the temperature of complete dissolution; therefore, these points belong to the HAZ_2 sub-zone where coarsening occurs.

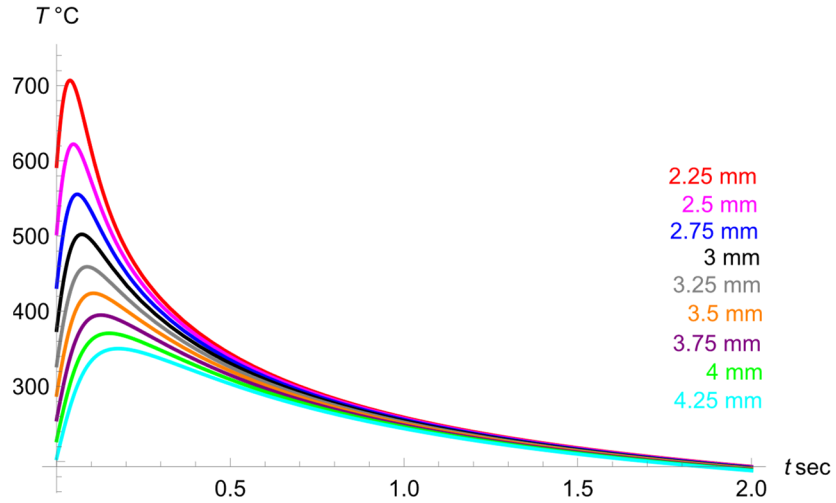

Figure 7. Calculated thermal cycles induced at various points on the HAZ. These points are depicted in Figure 5a in red. The legend indicates the y(mm) coordinate of each point.

3.3. Microhardness Tests Results

The microhardness tests results of the naturally aged samples are presented in Figure 8. The tests were carried out immediately after the heat treatment (0 h) and at intervals of 1 h up to 18 days afterward in order to investigate the effect of natural aging on the microhardness of the alloy.

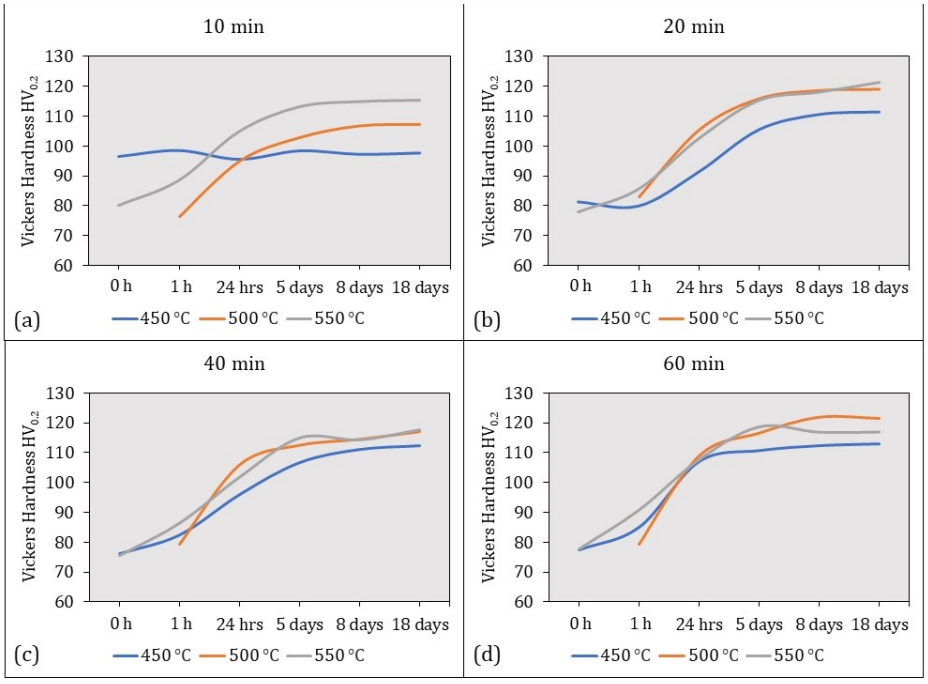

Figure 8. Microhardness test results for the solution heat-treated samples for hold times (**a**) 10 min, (**b**) 20 min, (**c**) 40 min and (**d**) 60 min. Afterward, the samples were naturally aged for various time intervals between 1 h and 18 days. Time 0 h indicates the tests performed immediately after the dissolution.

After the solution heat treatment, the microhardness of the alloy decreases from 150 $HV_{0.2}$ to about 80 $HV_{0.2}$ in almost all cases. The microhardness increases over time due to natural aging, reaching a mean value of 120 $HV_{0.2}$. Microhardness appears to stabilize after approximately 8 days.

As shown in Figure 9, the microhardness of the over-aged samples drops to 132 $HV_{0.2}$ after 8 h at 200 °C, while it stabilizes after approximately 48 h. For the samples heated to 250 °C, the microhardness decreases to 128 $HV_{0.2}$ after 2 h and stabilizes around 85 $HV_{0.2}$ after 24 h. For the samples heated to 300 °C, the decrease in microhardness is approximately 75 $HV_{0.2}$ after 8 h and stabilizes around 65 $HV_{0.2}$.

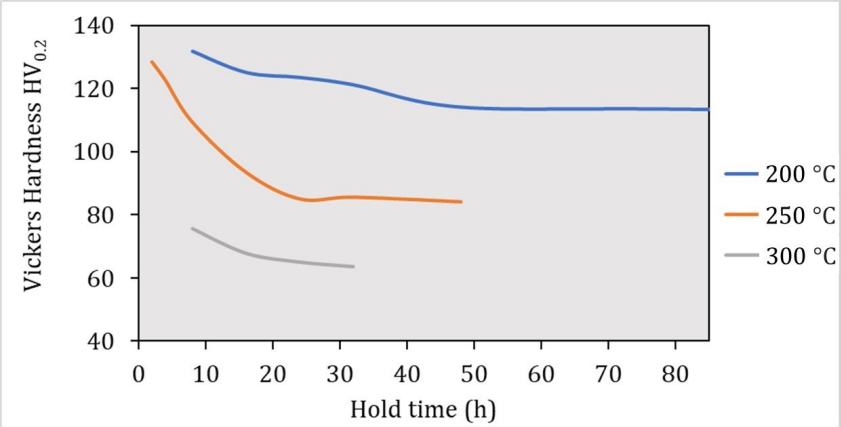

Figure 9. Microhardness test results for the overaged heat-treated samples.

4. Discussion

4.1. Simulation of the HAZ Microhardness Profile with Isothermal Heat Treatments

One of the objectives of this study is to replicate the microhardness profile of the HAZ with appropriate isothermal heat treatment schemes. In Figure 10, the HAZ microhardness profile is compared with the nearest microhardness values obtained through the heat treatments.

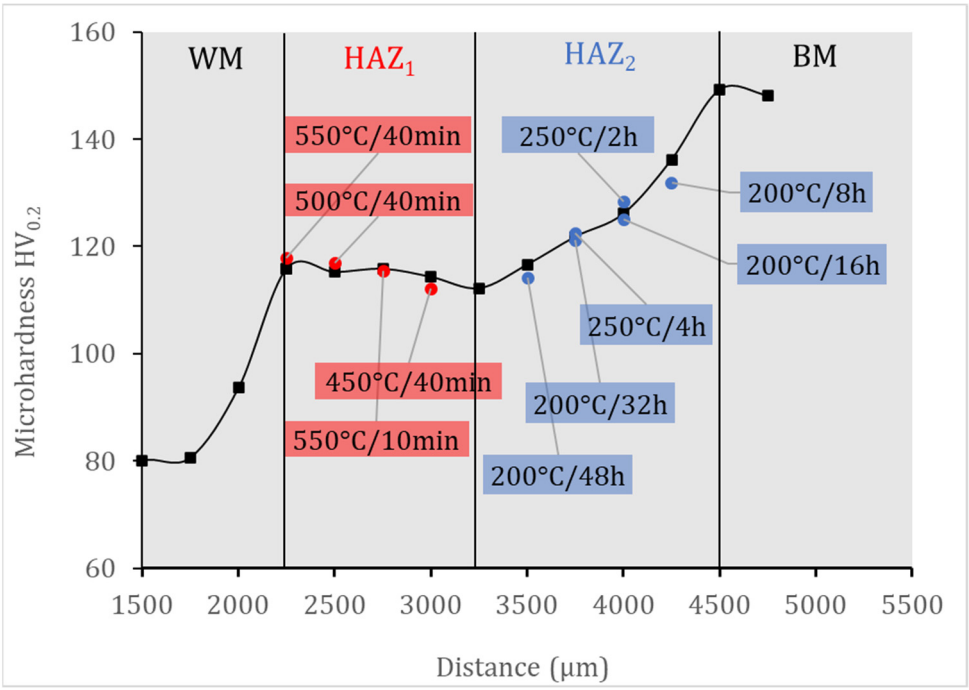

Figure 10. The microhardness profile of the weld seam compared to microhardness values resulting from isothermal heat treatments (red and blue points).

At the 2.25–3 mm region of the HAZ microhardness profile, the temperature during welding exceeded 493 °C (Figure 7); therefore, dissolution and precipitation occurred. The

microhardness of this zone (112–116 $HV_{0.2}$) can be simulated with solution heat treatments followed by natural aging, as shown in Figure 10, where the microhardness values of the isothermal treatments are correlated to the microhardness profile. At the 3.5–4.25 mm region, the maximum temperature did not exceed the temperature of complete dissolution (Figure 7); therefore, coarsening occurred. As shown in Figure 10, the microhardness profile of HAZ_2, ranging between 116–136 $HV_{0.2}$, can be sufficiently simulated by over-aging heat treatments. The heat treatments that closely correspond in value to the microhardness profile are 200 °C/48 h, 200 °C/32 h, 250 °C/4 h, 250 °C/2 h, 200 °C/16 h and 200 °C/8 h.

4.2. Correlation between Microhardness and Microstructure Changes

The reduction in the microhardness that occurs after dissolution/re-precipitation and coarsening are attributed to microstructure changes that involve the T_1 and θ′ precipitates. The TEM analysis of the as-received, naturally aged (after solution heat-treat 500 °C/20 min) and overaged (200 °C/48 h) material are presented in Figure 11.

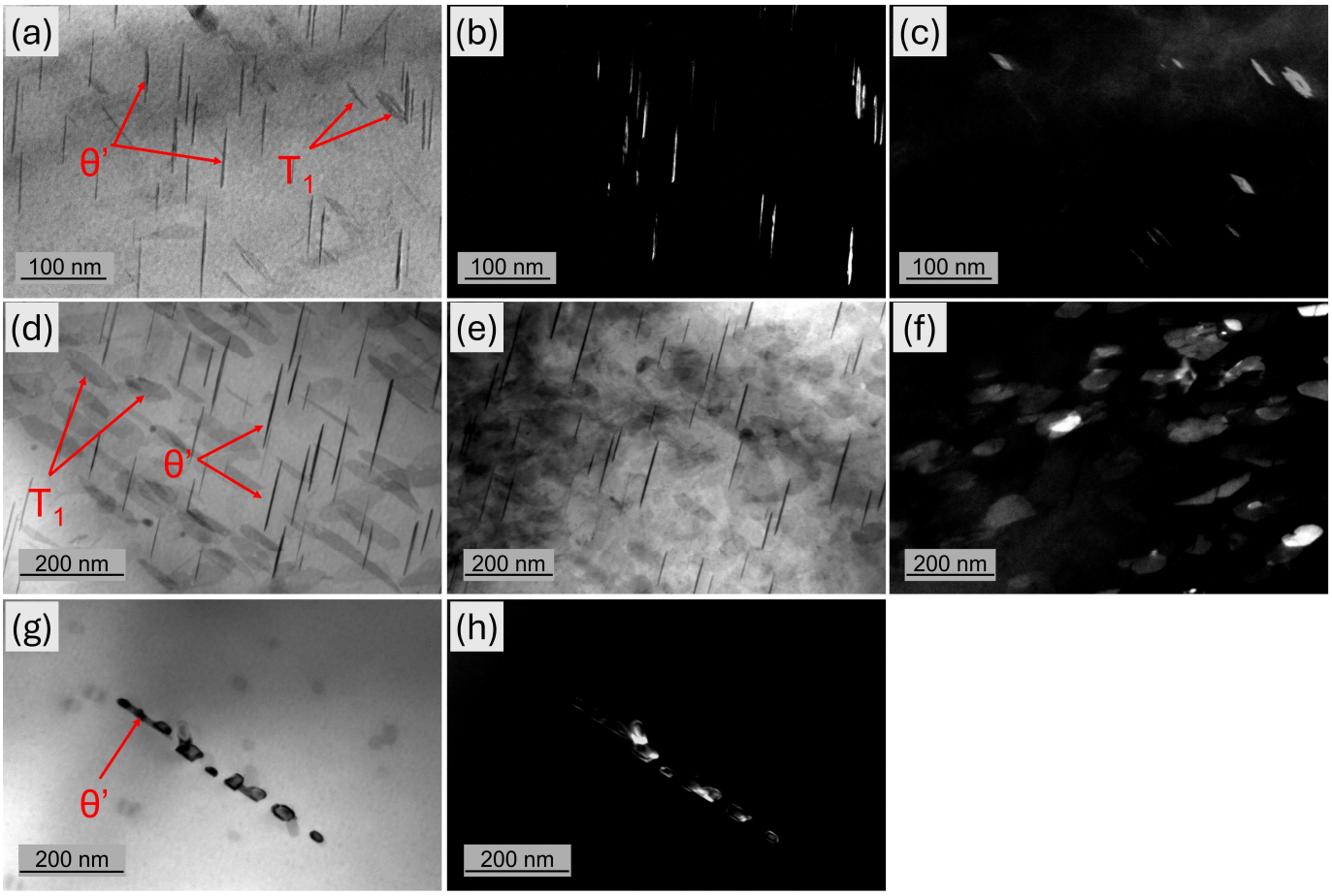

Figure 11. TEM BF and DF micrographs of (**a**–**c**) the as-received sample where θ′ and T1 phases are evident, (**d**–**f**) the solution heat treated at 500 °C for 20 min and naturally aged sample, (**g**,**h**) the overaged sample at 200 °C for 48 h.

As shown in Figure 11a–c, in the as-received state, two types of needle-shaped intermetallics crystallize with different orientations within the same grain. According to the EDS analyses, one type is θ′, whose length varies between 20–200 nm and whose mean width is 2.5 ± 0.6 nm. The second intermetallic is T_1, which shows a greater width (5.85 ± 2.3 nm) and a shorter length than θ′. After dissolution and natural aging (Figure 11d–f), two types of intermetallics are formed in the microstructure as well: θ′ and T_1. After re-precipitation, the mean width of θ′ is 4.86 ± 1.63 nm, which is slightly increased compared to the as-

received state. On the contrary, T_1 precipitates with a significantly increased mean width of 21.61 ± 9.25 nm, compared to T351 temper state. This is attributed to the fact that the formation of T_1 phase is dependent on the presence of dislocations, which is why pre-deformation favors the nucleation and precipitation of T_1 [44]. In the as-received state, the specimen, being in temper T351, has undergone cold deformation, while the solution heat-treated (500 °C/20 min) specimen has undergone dissolution and re-precipitation through natural aging without any pre-deformation. Previous studies have shown that the mean thickness of T_1 decreases with increasing pre-deformation [44]. Therefore, due to the absence of pre-deformation, T_1 precipitates with a significantly greater width, which leads to a reduction in microhardness. After over-aging, θ′ (Figure 11g,h) seems to prevail in the microstructure. The considerable difference in its mean width after overaging is evident, as from 2.5 nm in the as-received state, after heat treatment, the width increased to an average value of 25.5 ± 9 nm. This is to be expected, as over-aging leads to the coarsening of the strengthening phases, negatively affecting the microhardness. In Table 5, the mean width and volume fraction of the two strengthening phases are presented. Volume fractions were calculated through a two-dimensional method.

Table 5. Comparison of the mean width and volume fraction (f) of the θ′ and T_1 phases in three as-received, naturally aged and overaged conditions in combination with the microhardness values.

Phase	As-Received		HT 500 °C/20 min + Natural Aging		HT 200 °C/48 h	
	Width (nm)	**f (%)**	**Width (nm)**	**f (%)**	**Width (nm)**	**f (%)**
θ′ (Al_2Cu)	2.5 ± 0.6	3.42 ± 1.03	4.86 ± 1.63	2.59 ± 0.97	25.5 ± 9	3.42 ± 1.03
T1 (Al_2CuLi)	5.85 ± 2.3	1.17 ± 0.29	21.61 ± 9.25	8.46 ± 2.3	-	-
$HV_{0.2}$	150		119		114.2	

5. Conclusions

In the present work, the reduction of the HAZ microhardness in an AA2198-T351 LBW was simulated through isothermal heat treatments. The HAZ was divided into two subzones: HAZ_1 and HAZ_2. Within the first zone, the temperature field developing during welding exceeds the dissolution temperature of the main strengthening precipitates, so the material is subjected to aging. In HAZ_2, the temperature is lower than that limit, which leads to the coarsening of the strengthening phases (over-aging). In both cases, the microhardness decreases. To decide on the appropriate conditions (T, t) for the heat treatments, the thermal cycles at different points of the HAZ were calculated through the application of the Rosenthal solution, and ThermoCalc software (version 2022a) and Diffusion Module (DICTRA) (version 2022a) were utilized. Microhardness tests were performed on the naturally aged and over-aged samples, and the values were matched with the HAZ microhardness profile. Our conclusions are as follows:

1. The calculated temperature field in the weld seam matches the microhardness profile; therefore, the theoretical and experimental data are in agreement.
2. After solution heat-treatments and natural aging, the microhardness of the material decreases from 150 to approximately 120 $HV_{0.2}$ due to the re-precipitation of T_1 with significantly increased width.
3. After over-aging heat treatments, the width of θ′ phase is almost ten times higher compared to the as-received sample, which is responsible for the reduction in microhardness. Microhardness decreases at a faster rate as the temperature increases. At 200 °C, it decreased to the value of 112 $HV_{0.2}$ for 250 °C to 85 $HV_{0.2}$ and for 300 °C to 64 $HV_{0.2}$.
4. With appropriate isothermal heat treatments, the microhardness profile of the HAZ during LBW can be replicated accurately, implying that it is possible to fabricate samples for the experimental study of damage tolerance behavior in the HAZ.

Author Contributions: S.M. methodology, experimental investigation, validation, software, original draft preparation. S.D. methodology, investigation, review and editing. P.E.T. methodology, investigation, Validation, review and editing. A.D.Z. Conceptualization, methodology, supervision, Validation, review and editing. All authors have read and agreed to the published version of the manuscript.

Funding: This research received no external funding.

Data Availability Statement: The raw and processed data required to reproduce these findings cannot be shared at this time due to technical and time limitations. The data can be shared through direct contact with the corresponding author.

Acknowledgments: Acknowledgements to the Director of the Laboratory of Materials of the Department of Mechanical Engineering UTH G.N. Haidemenopoulos for providing the material and his support.

Conflicts of Interest: The authors declare no conflicts of interest.

References

1. Duan, S.-W.; Matsuda, K.; Wang, T.; Zou, Y. Microstructures and Mechanical Properties of a Cast Al–Cu–Li Alloy during Heat Treatment Procedure. *Rare Met.* **2021**, *40*, 1897–1906. [CrossRef]
2. Lv, K.; Zhu, C.; Zheng, J.; Wang, X.; Chen, B. Precipitation of T_1 Phase in 2198 Al–Li Alloy Studied by Atomic-Resolution HAADF-STEM. *J. Mater. Res.* **2019**, *34*, 3535–3544. [CrossRef]
3. Eswara Prasad, N.; Gokhale, A.A.; Wanhill, R.J.H. Aluminium–Lithium Alloys. In *Aerospace Materials and Material Technologies*; Prasad, N.E., Wanhill, R.J.H., Eds.; Springer: Singapore, 2017; pp. 53–72, ISBN 9789811021336.
4. Zhang, S.; Zeng, W.; Yang, W.; Shi, C.; Wang, H. Ageing Response of a Al–Cu–Li 2198 Alloy. *Mater. Des.* **2014**, *63*, 368–374. [CrossRef]
5. Hajjioui, E.A.; Bouchaâla, K.; Faqir, M.; Essadiqi, E. A Review of Manufacturing Processes, Mechanical Properties and Precipitations for Aluminum Lithium Alloys Used in Aeronautic Applications. *Heliyon* **2023**, *9*, e12565. [CrossRef]
6. Wu, H.; Wu, G.; Xiang, L.; Tao, J.; Zheng, Z.; Sun, J.; Li, W.; Huang, C.; Lan, X. Impact of Corrosion on the Degradation of the Mechanical Properties of 2195 and 2297 Al Alloys in the Marine Environment. *Metals* **2022**, *12*, 1371. [CrossRef]
7. Kramer, L.S.; Langan, T.J.; Pickens, J.R.; Last, H. Development of Al-Mg-Li Alloys for Marine Applications. *J. Mater. Sci.* **1994**, *29*, 5826–5832. [CrossRef]
8. Tsivoulas, D.; Prangnell, P.B. Comparison of the Effect of Individual and Combined Zr and Mn Additions on the Fracture Behavior of Al-Cu-Li Alloy AA2198 Rolled Sheet. *Met. Mater. Trans. A* **2014**, *45*, 1338–1351. [CrossRef]
9. Zou, Y.; Chen, X.; Chen, B. Corrosion Behavior of 2198 Al–Cu–Li Alloy in Different Aging Stages in 3.5 wt% NaCl Aqueous Solution. *J. Mater. Res.* **2018**, *33*, 1011–1022. [CrossRef]
10. Starke, E.A. Historical Development and Present Status of Aluminum–Lithium Alloys. In *Aluminum-Lithium Alloys*; Elsevier: Amsterdam, The Netherlands, 2014; pp. 3–26, ISBN 9780124016989.
11. Hirosawa, S.; Sato, T.; Kamio, A.; Flower, H.M. Classification of the Role of Microalloying Elements in Phase Decomposition of Al Based Alloys. *Acta Mater.* **2000**, *48*, 1797–1806. [CrossRef]
12. Jambor, M.; Nový, F.; Bokůvka, O.; Trško, L. The Natural Aging Behavior of the AA 2055 Al-Cu-Li Alloy. *Transp. Res. Procedia* **2019**, *40*, 42–45. [CrossRef]
13. Li, S.; Yue, X.; Li, Q.; Peng, H.; Dong, B.; Liu, T.; Yang, H.; Fan, J.; Shu, S.; Qiu, F.; et al. Development and Applications of Aluminum Alloys for Aerospace Industry. *J. Mater. Res. Technol.* **2023**, *27*, 944–983. [CrossRef]
14. Liu, S.; Wróbel, J.S.; LLorca, J. First-Principles Analysis of the Al-Rich Corner of Al-Li-Cu Phase Diagram. *Acta Mater.* **2022**, *236*, 118129. [CrossRef]
15. Li, Y.; Shi, Z.; Lin, J. Experimental Investigation and Modelling of Yield Strength and Work Hardening Behaviour of Artificially Aged Al-Cu-Li Alloy. *Mater. Des.* **2019**, *183*, 108121. [CrossRef]
16. Decreus, B.; Deschamps, A.; De Geuser, F.; Donnadieu, P.; Sigli, C.; Weyland, M. The Influence of Cu/Li Ratio on Precipitation in Al–Cu–Li–x Alloys. *Acta Mater.* **2013**, *61*, 2207–2218. [CrossRef]
17. Tao, Y.; Zhang, Z.; Xue, P.; Ni, D.R.; Xiao, B.L.; Ma, Z.Y. Effect of Post Weld Artificial Aging and Water Cooling on Microstructure and Mechanical Properties of Friction Stir Welded 2198-T8 Al-Li Joints. *J. Mater. Sci. Technol.* **2022**, *123*, 92–112. [CrossRef]
18. Zhao, T.; Sato, Y.S.; Xiao, R.; Huang, T.; Zhang, J. Hardness Distribution and Aging Response Associated with Precipitation Behavior in a Laser Pressure Welded Al–Li Alloy 2198. *Mater. Sci. Eng. A* **2021**, *808*, 140946. [CrossRef]
19. Gao, C.; Zhu, Z.; Han, J.; Li, H. Correlation of Microstructure and Mechanical Properties in Friction Stir Welded 2198-T8 Al–Li Alloy. *Mater. Sci. Eng. A* **2015**, *639*, 489–499. [CrossRef]
20. Cavaliere, P.; Cabibbo, M.; Panella, F.; Squillace, A. 2198 Al–Li Plates Joined by Friction Stir Welding: Mechanical and Microstructural Behavior. *Mater. Des.* **2009**, *30*, 3622–3631. [CrossRef]
21. Gao, C.; Ma, Y.; Tang, L.; Wang, P.; Zhang, X. Microstructural Evolution and Mechanical Behavior of Friction Spot Welded 2198-T8 Al-Li Alloy during Aging Treatment. *Mater. Des.* **2017**, *115*, 224–230. [CrossRef]

22. Zeng, Q.; Zeng, S.; Wang, D. Stress-Corrosion Behavior and Characteristics of the Friction Stir Welding of an AA2198-T34 Alloy. *Int. J. Miner. Met. Mater.* **2020**, *27*, 774–782. [CrossRef]
23. Texier, D.; Zedan, Y.; Amoros, T.; Feulvarch, E.; Stinville, J.C.; Bocher, P. Near-Surface Mechanical Heterogeneities in a Dissimilar Aluminum Alloys Friction Stir Welded Joint. *Mater. Des.* **2016**, *108*, 217–229. [CrossRef]
24. Rao, J.; Payton, E.J.; Somsen, C.; Neuking, K.; Eggeler, G.; Kostka, A.; Dos Santos, J.F. Where Does the Lithium Go?—A Study of the Precipitates in the Stir Zone of a Friction Stir Weld in a Li-containing 2xxx Series Al Alloy. *Adv. Eng. Mater.* **2010**, *12*, 298–303. [CrossRef]
25. Bitondo, C.; Prisco, U.; Squillace, A.; Giorleo, G.; Buonadonna, P.; Dionoro, G.; Campanile, G. Friction Stir Welding of AA2198-T3 Butt Joints for Aeronautical Applications. *Int. J. Mater. Form.* **2010**, *3*, 1079–1082. [CrossRef]
26. Li, W.; Jiang, R.; Zhang, Z.; Ma, Y. Effect of Rotation Speed to Welding Speed Ratio on Microstructure and Mechanical Behavior of Friction Stir Welded Aluminum–Lithium Alloy Joints. *Adv. Eng. Mater.* **2013**, *15*, 1051–1058. [CrossRef]
27. Ma, Y.E.; Xia, Z.C.; Jiang, R.R.; Li, W. Effect of Welding Parameters on Mechanical and Fatigue Properties of Friction Stir Welded 2198 T8 Aluminum–Lithium Alloy Joints. *Eng. Fract. Mech.* **2013**, *114*, 1–11. [CrossRef]
28. Examilioti, T.N.; Kashaev, N.; Enz, J.; Klusemann, B.; Alexopoulos, N.D. On the Influence of Laser Beam Welding Parameters for Autogenous AA2198 Welded Joints. *Int. J. Adv. Manuf. Technol.* **2020**, *110*, 2079–2092. [CrossRef]
29. Zhao, T.; Sato, Y.S.; Xiao, R.; Huang, T.; Zhang, J. Laser Pressure Welding of Al-Li Alloy 2198: Effect of Welding Parameters on Fusion Zone Characteristics Associated with Mechanical Properties. *High Temp. Mater. Process.* **2020**, *39*, 146–156. [CrossRef]
30. Yin, S.; Lü, J.; Xiao, R. Corrosion Behavior of Laser Beam Welded Joint of 2198 Aluminium-Lithium Alloy with Filler Wire. *Chin. J. Laser* **2016**, *43*, 0403007. [CrossRef]
31. Lin, K.; Yang, W.; Huang, T.; Xiao, R. Laser Welding of 2198-T851 Al-Li Alloy with Filler Wire. *Guang Xue Xue Bao* **2015**, *35*, s216001. [CrossRef]
32. Węgrzyn, T.; Piwnik, J.; Łazarz, B.; Wieszała, R.; Hadryś, D. Parameters of Welding with Micro-Jet Cooling. *Arch. Mater. Sci. Eng.* **2012**, *54*, 86–92.
33. Szczucka-Lasota, B.; Węgrzyn, T.; Krzysztoforski, M. Aluminum Alloys Welding with Micro-Jet Cooling in Busducts. *Weld. Tech. Rev.* **2018**, *91*, 24–30. [CrossRef]
34. David, S.A.; Babu, S.S.; Vitek, J.M. Welding. In *Encyclopedia of Materials: Science and Technology*; Elsevier: Amsterdam, The Netherlands, 2003; pp. 1–9, ISBN 9780080431529.
35. Song, W.; Man, Z.; Xu, J.; Wang, X.; Liu, C.; Zhou, G.; Berto, F. Fatigue Crack Growth Behavior of Different Zones in an Overmatched Welded Joint Made with D32 Marine Structural Steel. *Metals* **2023**, *13*, 535. [CrossRef]
36. Song, Y.; Chai, M.; Han, Z. Experimental Investigation of Fatigue Crack Growth Behavior of the 2.25Cr1Mo0.25V Steel Welded Joint Used in Hydrogenation Reactors. *Materials* **2021**, *14*, 1159. [CrossRef] [PubMed]
37. Smaili, F.; Lojen, G.; Vuherer, T. Fatigue Crack Initiation and Propagation of Different Heat Affected Zones in the Presence of a Microdefect. *Int. J. Fatigue* **2019**, *128*, 105191. [CrossRef]
38. Tzamtzis, A. *Fatigue Crack Growth Prediction under Mode I Loading in Friction Stir Aluminum Alloy Weld*; University of Thessaly, School of Engineering, Department of Mechanical Engineering: Volos, Greece, 2015.
39. Kim, S.; Kang, D.; Kim, T.-W.; Lee, J.; Lee, C. Fatigue Crack Growth Behavior of the Simulated HAZ of 800MPa Grade High-Performance Steel. *Mater. Sci. Eng. A* **2011**, *528*, 2331–2338. [CrossRef]
40. Vriami, D. Experimental Study of Welding of New Aircraft Aluminum Alloys with High Power Beams (LBW, EBW). Diploma Thesis, Department of Mechanical Engineering, University of Thessaly, Volos, Greece, 2010. (In Greek)
41. Zervaki, A.D.; Haidemenopoulos, G.N. Computational Kinetics Simulation of the Dissolution and Coarsening in the HAZ during Laser Welding of 6061-T6 Al-Alloy. *Weld. Res.* **2007**, *86*, 211–221.
42. Andersson, J.-O.; Helander, T.; Höglund, L.; Shi, P.; Sundman, B. Thermo-Calc & DICTRA, Computational Tools for Materials Science. *Calphad* **2002**, *26*, 273–312. [CrossRef]
43. Masubuchi, K. *Analysis of Welded Structures*; Elsevier: Amsterdam, The Netherlands, 1980; pp. 60–71, ISBN 9780080227146.
44. Yang, Y.; He, G.; Liu, Y.; Li, K.; Wu, W.; Huang, C. Quantitative Contribution of T1 Phase to the Strength of Al-Cu-Li Alloys. *J. Mater. Sci.* **2021**, *56*, 18368–18390. [CrossRef]

Disclaimer/Publisher's Note: The statements, opinions and data contained in all publications are solely those of the individual author(s) and contributor(s) and not of MDPI and/or the editor(s). MDPI and/or the editor(s) disclaim responsibility for any injury to people or property resulting from any ideas, methods, instructions or products referred to in the content.